Octopus-inspired Eight-arm Robotic Swimming by Sculling Movements

Michael Sfakiotakis, Asimina Kazakidi, Nikolaos Pateromichelakis and Dimitris P. Tsakiris

Abstract— Underwater robotic devices, equipped with manipulator arms, usually employ propellers or impellers to propel themselves through the fluid medium. Their robotic functionality and robustness, however, could be greatly enhanced by the use of multi-function manipulators, which, besides their manipulation capabilities for performing dexterous robotic tasks, could also provide propulsion. Inspired by the octopus arm morphology and exploiting recordings of swimming octopus, we investigate the propulsive capabilities of an eight-arm robotic system under various swimming gaits, including arm sculling and arm undulations, for the generation of forward and turning movement. A dynamical model of the robotic system, that considers fluid drag contributions accurately evaluated by computational fluid dynamic methods, was used to study the effects of various kinematic parameters on propulsion. Underwater experiments in a water tank, employing several eight-arm prototype devices, demonstrated their three-dimensional free-swimming capabilities, achieving a maximum speed of approximately 0.2 body lengths per second. Similar trends were observed, as in the simulation studies, with respect to the effect of the kinematic parameters on propulsion.

Index Terms— Biologically-Inspired Robots, Underwater Propulsion, Hydrodynamics, Octopus.

I. INTRODUCTION

Compliant robotic manipulators have been inspired by the outstanding locomotor and manipulation capabilities of the octopus. This coleoid uses swimming as a means of locomotion for hunting, defense, or escape. Several swimming patterns have been recognized in the wild [1] or the aquarium [2], but during *arm swimming*, in particular, the octopus appears to generate considerable propulsive speed and rapid acceleration. This motion pattern involves the synchronous movement of all eight arms (Fig. 1), which resembles the *sculling* swimming motion, and is composed of two distinct parts: one where the arms are opening relatively slowly (recovery stroke) and one where they are closing fast (power stroke). Significant forward thrust is generated during the latter part of the movement, i.e., the power stroke [1], [2]. This motion pattern possesses remarkable symmetry, since the arrangement of the eight octopus arms is symmetrical and their movement is synchronized.

Such propulsion capabilities could be adopted in underwater robotic devices, equipped with flexible, multi-function manipulators, analogous to the octopus arms, which could be used both for manipulation [3]–[6] and propulsion. Such a system could serve sophisticated robotic applications in underwater search-and-rescue operations, inspection of submerged industrial pipelines and undersea exploration. A preliminary study of a 2-arm planar robotic swimmer [7], emulating octopus arm swimming, exploited the above-mentioned symmetry of this swimming pattern, and demonstrated some basic aspects of it.

In the present paper, an 8-arm robotic swimmer was developed, to investigate the propulsive ability of such a system under various swimming gaits. The dynamical model was developed, which incorporated accurate fluid drag data obtained by computational fluid dynamic (CFD) methods. These CFD studies employed realistic arm-like structures embedded in fluid flow, specifying the associated fluid drag coefficients and mean values for the normalized normal and tangential force coefficients for various configurations of segmented sculling arms. We examined arm sculling and arm undulations, as well as combinations thereof, for the generation of forward and turning movements, and the effect of various kinematic parameters on these gaits. A prototype robotic device, swimming by the coordinated movement of its 8 arms, was also developed to investigate the applicability of the model. Parametric studies on the prototype showed trends similar to the simulation results.

Section II of the paper presents the biological background of the octopus arm swimming locomotion, and CFD data on the 1-arm sculling motion. Section III describes the Matlab-based computational model developed to simulate various swimming gaits of the robotic 8-arm swimmer. A series of simulations, which include a parametric study of the effect of the various kinematic parameters on propulsive speed is given in Section IV. Section V describes the experimental testbed, and Section VI presents the experimental studies and the obtained results.

M. Sfakiotakis, A. Kazakidi, N. Pateromichelakis, and D.P. Tsakiris are with the Institute of Computer Science, Foundation for Research and Technology – Hellas (FORTH), N. Plastira 100, Vassilika Vouton, GR-70013, Heraklion, Greece. M. Sfakiotakis is also with the Dept. of Electrical Engineering, Technological Educational Institute of Crete, Heraklion, Greece. {sfakios, kazakidi, nikospat, tsakiris}@ics.forth.gr.
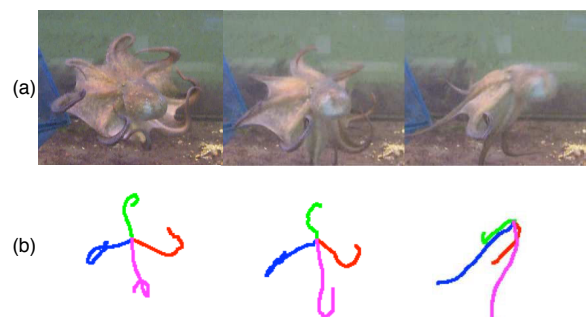

Fig. 1: (a) Snapshots of octopus arm swimming motion [2]. (b) Two-dimensional projections of four arms during the movement.
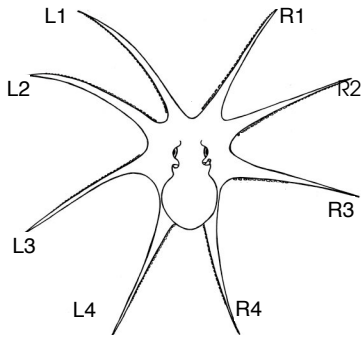
Fig. 2: The octopus body and anatomical arm notation. [8]

II. BACKGROUND STUDIES

A. Biological observations

Benthic and deep-water octopuses use several swimming modes to propel themselves above the seabed [1]. Although the predominant one appears to be *jet swimming*—which involves usage of the siphon with the arms trailing tightly behind the head and the mantle—, *arm swimming* is the only mode in which the octopus actively employs all eight arms, in a synchronized and coordinated manner [2]. It is noted that the web, the siphon and the mantle orientation may also play a role during the movement, e.g., for steering or for buoyancy control, but the primary thrust generation mechanism is attributed to the motion of the arms. The standard anatomical notation to the octopus arms is as shown in Fig. 2. Video recordings of the arm swimming mode on two *Abdopus aculeatus* in the wild [1] and five *Octopus vulgaris* in captivity (Fig. 1) [2] suggest a ratio between recovery stroke (T_r) and power stroke (T_p) durations of approximately 2.5 ± 0.5 for both species.

B. Single-arm sculling motion

A first, simplified approximation of the octopus arm-swimming motion considers the arms performing a two-stroke motion (with a velocity ratio β between the power and recovery strokes) while rotating as straight units around their bases. We term this mode as *sculling*.

Sculling was first examined on a 1-arm system with the use of CFD methods, the details of which can be found in [9]. The sculling profile for arm rotation angle $\varphi(t)$ is characterized by the sculling amplitude A, the sculling offset ψ, the recovery (base) velocity ω and the velocity ratio β (Fig. 3a, red line in Fig. 3b). The geometry was identical to the one used for the robotic arms of the prototype developed for this study (see Section V). The CFD simulations showed that the non-dimensional x-component of the total force ($\tilde{F}_x$) has a positive time-integral (dashed blue line in Fig. 3b), thus confirming the generation of forward thrust. The simulations also depict in detail the complexity of the fluid field developed around the moving arm (Figs. 3c-d).

III. SIMULATION STUDIES

A. Eight-arm mechanical model

The 8-arm mechanism used to study various swimming gaits and shown in Fig. 4 is considered, comprising eight arm-like appendages, attached to the rear side of a main body segment. Each arm is modelled as a kinematic chain of $n = 10$ cylindrical rigid segments, interconnected by 1-dof planar rotary joints. The arms are symmetrically arranged, at $45°$ intervals, around the circumference of a circle with radius R, and are oriented so that each pair of diametrically-placed arms moves in the same plane, as illustrated in Fig. 5.

B. Fluid drag model

The fluid drag model, used in SIMUUN to simulate the interaction of the arm segments with the aquatic environment, is a first approximation of the hydrodynamics involved, assuming that: (i) fluid forces are mainly inertial (roughly for a Reynolds number $400 < Re < 4 \cdot 10^5$), (ii) the fluid is stationary, so that its force on a single segment is due only to the motion of that segment, and (iii) the tangential (F_T), normal (F_N) and lateral (F_L) components of the fluid force are decoupled. These are then calculated, for individual segments as:

$$F_{\mathrm{dir}}^i = -\lambda_{\mathrm{dir}}^i \, \mathrm{sgn}(v_{\mathrm{dir}}^i) \cdot (v_{\mathrm{dir}}^i)^2, \, \mathrm{dir} = \{T, N, L\} \quad (1)$$
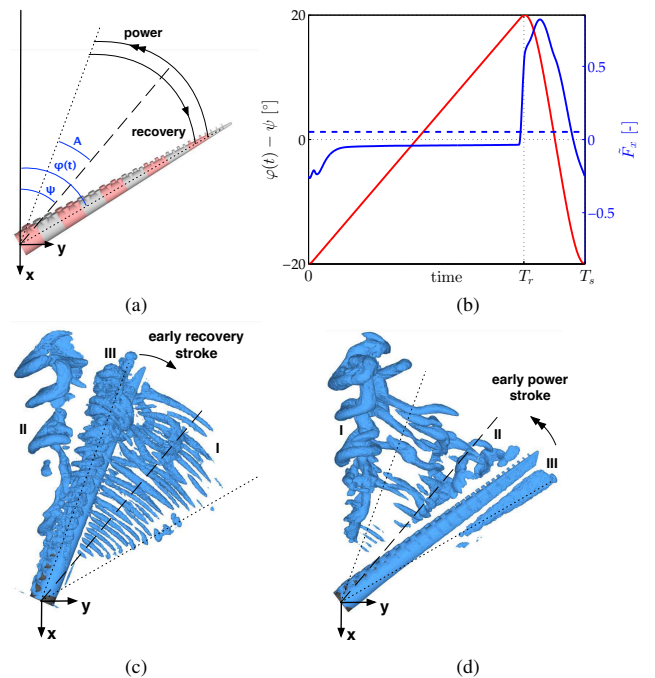

Fig. 3: CFD study of single-arm sculling motion. (a) Definition of kinematic parameters. (b) Angular displacement over time (red); force $\tilde{F}_x$ (blue) with a positive average value (dashed line). (c-d) Vortical patterns visualized by λ_2 isocontours [10]: (c) $t = 0.08 T_s$, (d) $t = 0.92 T_s$, near max $\tilde{F}_x$ ($A = 20^o$, $\psi = 40^o$, $\omega = 50^o/s$, $\beta = 5$). Vortices in (c) are generated at (I): previous T_p, (II): end of T_p, III: beginning of T_r. Vortices in (d) are due to (I): previous end of T_p, (II): previous T_r, (III): beginning of new T_p.
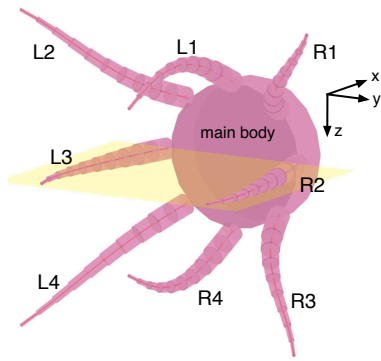
Fig. 4: Configuration of the 8-arm swimming mechanism, indicating the common motion plane between a pair of diametrically opposite arms.
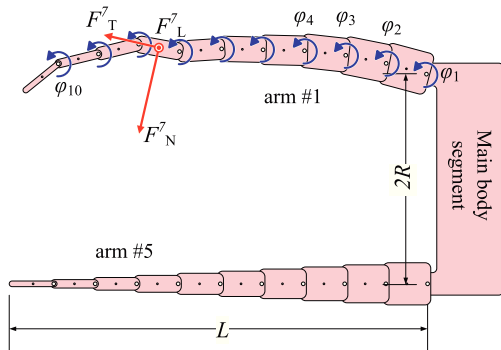

Fig. 5: Planar view of a pair of diametrically-placed arms.

where v_T^i, v_N^i and v_L^i are the tangential, normal and lateral components, respectively, of the velocity of the ith segment, while λ_T^i, λ_N^i and λ_L^i denote the segment's drag coefficients associated with each force component. Due to the axial symmetry of the segments, the normal and lateral coefficients are equal, i.e., $\lambda_N^i = \lambda_L^i$. The use of such a resistive fluid force model dates back to the study of the undulatory swimming of elongate animals in [11], and has since been widely adopted in the analysis of similarly-shaped bio-inspired robotic underwater systems (see, e.g., [12]–[14]). Further evidence for the validity of this approach, at least for the type of arm movements considered in the present study, was obtained by the computational fluid dynamics (CFD) investigations presented in [7], the results of which were also used to obtain estimates for the fluid drag coefficients in (1).

IV. SIMULATION RESULTS

A computational model of the above 8-arm mechanism has been implemented in the SIMUUN simulation environment, which is based on the SimMechanics toolbox of Simulink. The configuration and mechanical parameters (dimensions, masses, inertias, etc.) for the arms and the main body were specified to reflect those of the prototype employed in the experimental studies (see Section V). In the developed model, internal changes of the arms' shape are imposed by explicitly prescribing angular trajectories for the mechanism's rotary joints φ_i^j, while the arms' interaction with the aquatic environment is described using the simple fluid
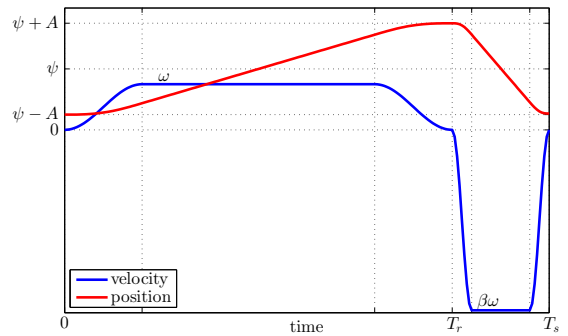

Fig. 6: Sculling motion profile.

drag model presented in Section III-B, where the values of the associated fluid drag coefficients for each of the arm segment were specified from the CFD analysis in [7]. The drag coefficients associated with the main body of the mechanism were estimated using standard fluid mechanics formulas for flow over a circular disk.

This framework was employed to study a range of multi-arm propulsion modes, proposed as a first approximation to capture the main aspects of the octopus' multi-arm swimming. These modes are essentially extensions to 8-arm mechanisms moving in 3D, of the ones originally proposed in [7]. Specifically, we initially study the sculling mode and then its combination with undulatory arm motions. Our studies also consider a number of variants of these basic propulsion modes, and the implementation of turning, as well as forward gaits.

A. Sculling forward movement

In the proposed sculling mode, each arm oscillates as a single straight unit, by setting $\varphi_i = 0$ for the inter-segment joints ($i = 2..n$), while prescribing a two-stroke periodic angle variation for the joint connecting the arm to the main body. In the present study, the trajectories of both the recovery and the power stroke are obtained using a sinusoidal motion profile, where the velocity is maintained at its maximum value for 60% of the stroke's duration (Fig. 6). Such a profile generates smooth trajectories, thus facilitating their implementation through the actuators employed in the experimental platform (see Section V). The parameters of the sculling profile are as described in Section II-B. Denoting by T_p and T_r the duration of the power and the recovery stroke, respectively, the overall period of each stroke of the sculling motion will be $T_s = T_p + T_r = (\beta + 1)T_p$.

Forward movement along an approximately straight line may be generated by sculling movements of the robots arms, employing a variety of patterns of arm coordination. These give rise to patterns of swimming behavior, which, for convenience, will be termed "gaits". (This does not imply that transitions among these gaits occur at different velocities, as e.g., in horse gaits). The phase characteristics of the patterns of arm coordination, that give rise to each of the gaits described below, are summarized in Table I, which indicates the phase of each of the arms (as a fraction of the stride period T_s) with respect to arm L1.

TABLE I: Definition of sculling swimming gaits with arm coordination patterns

	Arm phase (as fraction of T_s with respect to L1)							
Gait	L1	L2	L3	L4	R1	R2	R3	R4
G1	0	0	0	0	0	0	0	0
G2	0	3/4	1/2	1/4	1/4	1/2	3/4	0
G3	0	0	3/4	3/4	1/4	1/4	1/2	1/2
G4	0	1/2	0	1/2	1/2	0	1/2	0
G5	0	1/2	1/2	0	0	1/2	1/2	0

G1 gait: The most straightforward arm coordination pattern is when all eight arms move in synchrony. The arm trajectories are shown in Fig. 7a. This gait is the only one observed in live octopuses.

G2 gait: This gait is produced by the synchronized sculling movement of pairs of diagonally opposite arms with a phase difference of $T_s/4$ between adjacent pairs of arms. The trajectories of the 4 pairs of arms are shown in Fig. 7b. This gait gives rise to a fast and smooth movement of the robot.

G3 gait: This gait is produced by the synchronized sculling movement of pairs of adjacent arms, in addition to a phase difference of $T_s/4$ between adjacent pairs of arms. This gives rise to a relatively slow and wobbling movement of the robot.

G4 gait: This gait is produced by the synchronized sculling movement of two sets of four arms, one set containing arms L1, L3, R2, R4 and the other arms L2, L4, R1, R3. There is a phase difference of $T_s/2$ between the two sets of arms. The trajectories of the 2 sets of arms are shown in Fig. 7c.

G5 gait: This gait is produced by the synchronized sculling movement of two sets of four arms, one set containing arms L1, L4, R1, R4 and the other arms L2, L3, R2, R3. There is a phase difference of $T_s/2$ between the two sets of arms.

In the above gaits, the action of the arms is equally distributed over the whole duration of the stride period T_s. Numerous variations of the above gaits are, evidently, possible, by e.g. altering the phase between the arms, so that their action is no longer equally distributed over T_s.

Indicative simulation results, demonstrating forward propulsion by gaits $G1$, $G2$ and $G4$, are shown in Fig. 7, for $A = 25°$, $\psi = 40°$, $\omega = 60°/\mathrm{s}$, and $\beta = 5$. These indicate that, although the average steady-state velocity V is approximately the same for the three gaits, the different patterns for the coordination of the arms' sculling motion have a significant impact on the characteristics of the system's instantaneous velocity $v_b(t)$. More specifically, in gait $G1$, the motion is more discontinuous, with $v_b(t)$ exhibiting quite pronounced peaks, that coincide with the occurrence of the power stroke by the arms' synchronised sculling motions. On the other hand, the phasing of the arms' power strokes in $G2$ results in thrust generation being evenly distributed over the duration of T_s. This is reflected in the velocity profile of the system, as the variations of $v_b(t)$, which occur with a period equal to $T_s/4$, are considerably reduced, and the overall forward motion of the system is much smoother. Correspondingly, the phasing of gait $G4$ yields a velocity profile with characteristics that fall in-between those of the other two gaits.

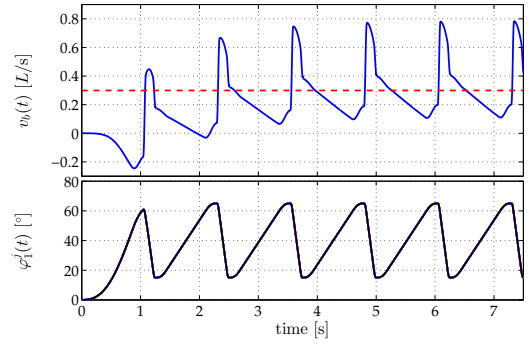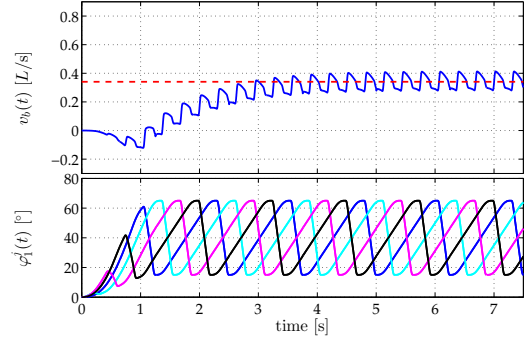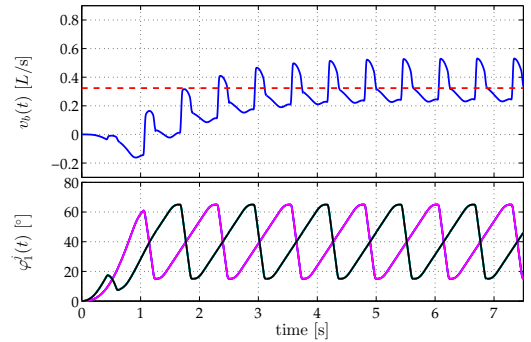Furthermore, the effect of the various parameters of the

(a) gait $G1$

(b) gait $G2$

(c) gait $G4$

Fig. 7: Simulation results: Instantaneous axial velocity (normalized by the arm length L) of the main body segment, shown against the arms' sculling trajectories, for gaits $G1$, $G2$, and $G4$. In each velocity plot, the dashed red line indicates the average steady-state velocity.

sculling motion profile has been investigated by a series of simulation runs, performed mainly with the $G1$ gait, over the range $5° \leq A \leq 35°$, $20° \leq \psi \leq 80°$. The results are summarized in Fig. 8, and indicate that, with the employed sculling profile, for constant ω, the average attained velocity V assumes its largest values for $\psi \approx 40°$, while there is a relatively smaller dependence on the sculling amplitude, when the latter is $A \geq 15°$. These observations are, for the most part, consistent with the ones presented for the 2-arm mechanism in [7]. Moreover, additional simulations (not shown here), confirmed the (intuitive) prediction that V increases with ω and β. Finally, it is noted that, although

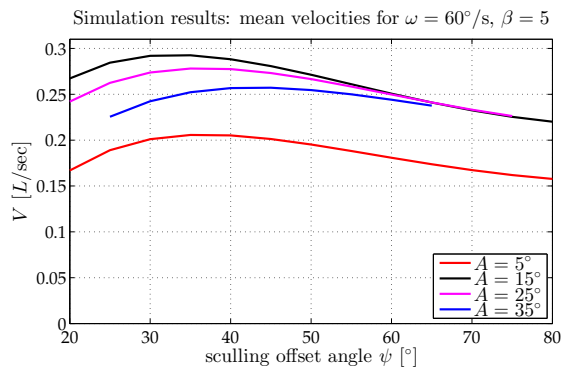Simulation results: mean velocities for $\omega = 60°/s$, $\beta = 5$

Fig. 8: Simulation results for gait $G1$: Variation of the average attained forward velocity, as a function of the sculling offset ψ, for different values of the sculling amplitude A.

the above results were obtained with gait $G1$, the findings also apply to $G2$ and $G4$, as suggested by the fact that the average attained velocity, for the same kinematic parameters, is about the same for all three gaits (cf. Fig. 7).

B. Sculling combined with arm undulations

Another possible swimming mode is a combination of sculling with arm undulations, which resembles better the octopus movement and was first presented in [7], for a 2-arm swimmer. Here, we extend and adapt this mode to the 8-arm swimmer. The mode characteristic is a traveling wave that propagates from the arm base towards the arm tip.

The travelling wave is implemented by prescribing sinusoidal oscillations for the joint angles of the arm segments [15], [16], according to:

$$\varphi_i^j(t) = B_i^j \sin\left(\frac{2\pi}{T_u^j}t + (i-2)k^j\frac{2\pi}{n} + \chi^j\right) \quad (2)$$

where, for the jth arm ($j = 1...8$), B_i^j is the oscillation amplitude of the ith segment ($j = 1...n$), T_u^j is the oscillation period, and k^j represents the number of wavelengths propagating on the arm. The relative timing between the undulation and the sculling for each arm is adjusted through the phase shift χ^j. Evidently, many different schemes are possible for prescribing the travelling wave shape, as well as for combining undulations with sculling. In the present study, we have restricted our investigations to travelling waves characterized by a common oscillation amplitude B for all the segments, and we have specified the period of the segments' oscillation to equal that of the sculling motion, by setting $T_u^j = T_s$, while gait $G1$ has been used for the sculling component of the arms' motion. Moreover, in order to obtain forward locomotion along a straight line, opposite arms perform these combined movements in anti-phase, thus ensuring the cancellation of sideforces.

The average attained velocity of the mechanism, as a function of the number of undulatory waves k, and for different values of the undulation amplitude B, is shown in Fig. 9, where the dashed line ($B = 0°$) corresponds to the velocity obtained by pure sculling. These results indicate that, for appropriate parameter choices, the combination of

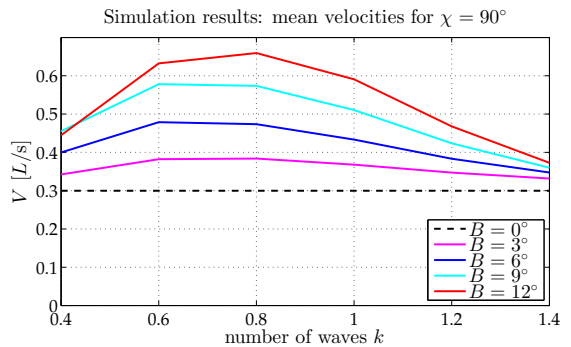Simulation results: mean velocities for $\chi = 90°$

Fig. 9: Simulation results for sculling combined with undulations: Average attained velocities for a varying number of wavelengths propagating along the arms, and for different oscillation amplitudes. The dashed line ($B = 0°$) corresponds to the sculling-only case. Sculling parameters were specified as $A = 10°$, $\psi = 40°$, $\omega = 60°/s$.

undulations with sculling can yield significant performance enhancements, in terms of the attained velocity.

C. Turning movements

In general, any asymmetry in the relative motion between the arms will tend to cause deviations of the robot from a straight path. Turning may, therefore, be instigated by a number of different strategies, which involve specifying different values for one (or more) parameters of the arms' motions. An example of one such strategy is shown in Fig. 10, where the system performs a turn on the xy plane by specifying the sculling/undulation phase shifts χ^j equal to $0°$ for {L1, R4}, $-80°$ for {L2, L3, L4}, and $80°$ for {R1, R2, R3}, while keeping the other parameters of the arms' motion fixed (Sculling parameters: $A = 10°$, $\psi = 35°$, $\omega = 60°/sec$, $\beta = 5$. Undulation parameters: $B = 12°$, $k^j = 0.8$).

V. EXPERIMENTAL SETUP

In order to experimentally investigate underwater propulsion by the various sculling gaits proposed in this study, the 8-arm robotic prototype shown in Fig. 11 was developed. The arms' geometry was approximated as a frustum with 20 mm in base diameter, 2 mm in tip diameter, and 200 mm
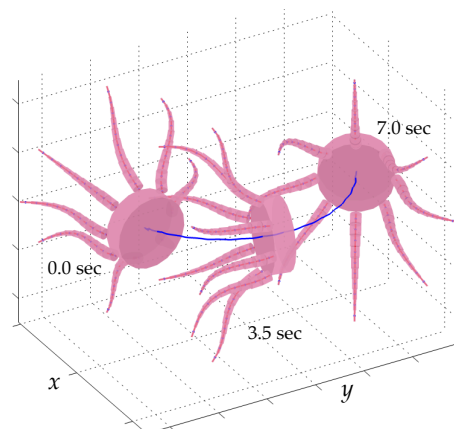

Fig. 10: Simulation result for turning movement with a combination of sculling and arm undulations.
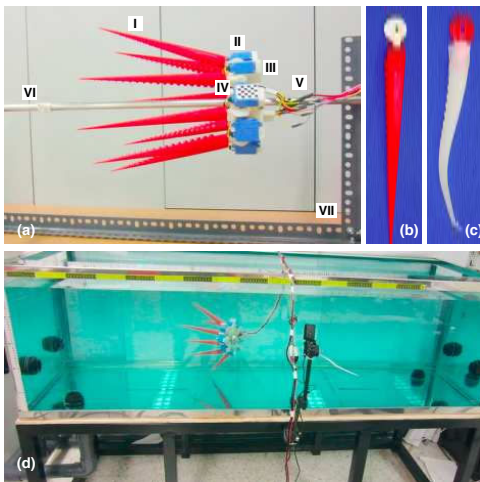
Fig. 11: (a) 8-arm robotic prototype: (I) arms, (II) servomotors, (III) platform, (IV) chequerboard marker, (V) connection cables, (VI) axial rod, and (VII) mounting frame. (b) Rigid arm. (c) Compliant arm. (d) Water tank.

in length, including 19 pairs of cylindrical protrusions in a staggered pattern, which represented the octopus suckers [9]. Two types of arms were fabricated: rigid arms (Figs. 11a-I, b) made from ABSplus using a 3D printer (Elite, Dimension, USA) and compliant arms (Fig. 11b) made from soft silicone rubber (Dragon Skin Q). Each arm was mounted on a dedicated waterproof micro-servomotor (HS-5086WP, Hitech, USA) capable of rotating the arm over a $90°$ span, in the configuration of Fig. 4. The 8 servomotors (Fig. 11a-II) were mounted on an octagonal platform (Fig. 11a-III) of diameter 15.5 cm (also fabricated using the 3D printer). The servomotors were controlled by an off-board microcontroller platform (*Arduino pro mini*), programmed to implement the appropriate arm trajectories for each one of the gaits under investigation. The overall weight of the prototype, after being submerged in the water for some time, was 700 gr. Experiments were performed with the mechanism inside a water tank of dimensions 200 cm (length) x 70 cm (width) x 60 cm (height), which was filled with tap water at room temperature (Fig. 11d).

The 3D underwater trajectory of the platform of the robotic swimmer was estimated by computer vision methods. A camera was fixed outside the glass wall of the water tank and was calibrated intrinsically, to remove lens distortion. A planar chequerboard marker (Fig. 11a-IV) of known size was attached to the platform, so as to be visible by the camera during the motion of the robot. The method used for estimating the position and orientation of the marker in each camera frame, first, calculated the homography between the camera's image plane and the marker's plane, up to a scale factor. Using this homography as an initial guess, the maximum likelihood estimate of the position and orientation of the marker was obtained by nonlinear minimization [17].

VI. EXPERIMENTAL RESULTS

In a first set of experiments, the 8-arm prototype, with the use of a linear bearing, was initially allowed to slide
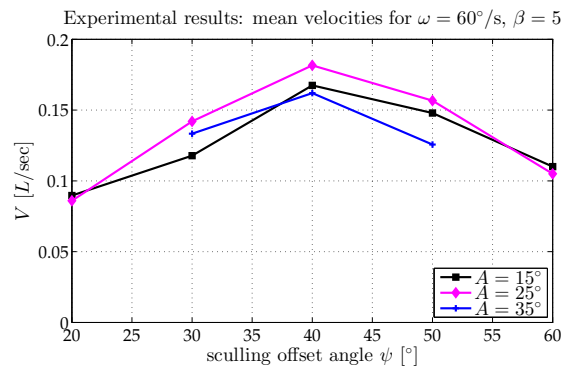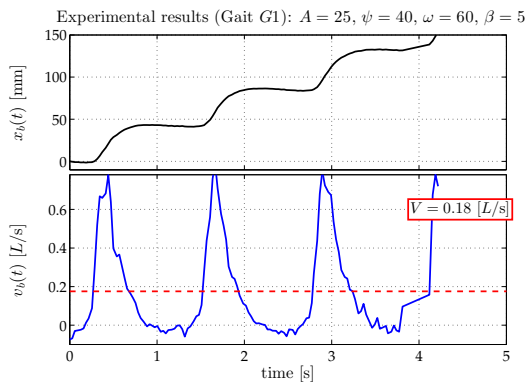

Fig. 12: Experimental results of horizontally constraint swimmer with rigid arms, for gait $G1$: Variation of the average attained forward velocity, as a function of the sculling offset ψ, for different values of the sculling amplitude A.

along a straight stainless steel rod (Fig. 11a-VI), which was mounted on a supporting frame resting at the bottom of the tank (Fig. 11a-VII). This constrained the robot swimmer to move along a horizontal axis, in order to investigate, in a systematic and controlled setting, the differences among the various gaits, as well as the influence of kinematic parameters on propulsion. In a second set of experiments, the prototype was passively regulated to hover at a constant depth within the tank and it was tested under free-swimming conditions, with both rigid and compliant arms.
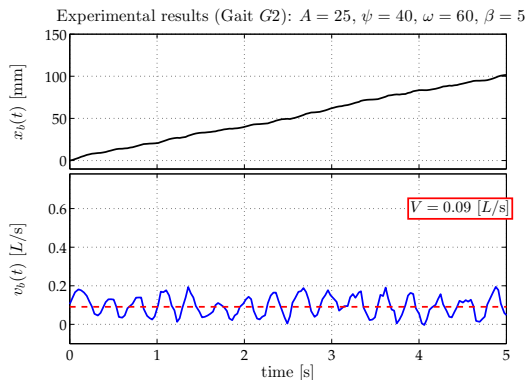
A. Horizontally constrained propulsion results

Initial experiments with the prototype, constrained to slide horizontally along the supporting rod, involved a series of tests with gait $G1$ over a range of sculling offsets and sculling amplitudes. The obtained results, with regard to the average attained velocity are provided in Fig. 12. Much like in the corresponding simulation results of Fig. 8, the optimal value of the offset angle was found to lie around $40°$, although the magnitude of the experimentally obtained velocities is reduced, compared to the predictions of the simulations. For the most part, these discrepancies should be attributed to the friction between the mechanism and the sliding rod, which dissipates a considerable portion of the propulsive energy generated by the arms' motions.
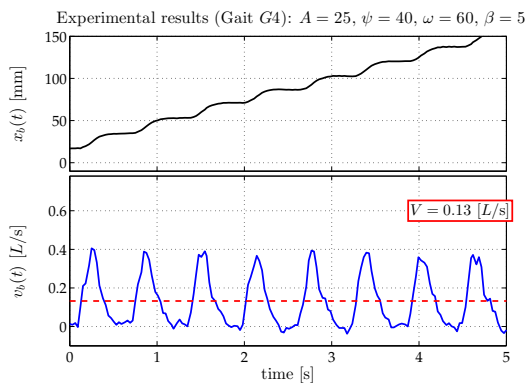
Regarding the different sculling gaits investigated here, Fig. 13 shows the temporal variation of the mechanism's axial velocity, derived from the displacement data (as obtained by the visual tracking system), for gaits G1, G2, and G4 (with the same sculling parameters). For all three gaits, significant qualitative agreement can be observed between these velocity profiles and those from the corresponding simulation results (Fig. 7), mainly relating to the overall shape and occurrence frequency of the velocity impulses. It can also be observed that, unlike in the simulations, there is a notable difference between the mean attained velocities among the three gaits, with $V_{G1} > V_{G4} > V_{G2}$. This should also be attributed to friction, when considering its magnitude in relation to the magnitude of the propulsive force impulses generated by the distinct activation pattern by a different number of

Experimental results (Gait $G1$): $A = 25$, $\psi = 40$, $\omega = 60$, $\beta = 5$

$V = 0.18 \; [L/s]$

(a) gait $G1$

Experimental results (Gait $G2$): $A = 25$, $\psi = 40$, $\omega = 60$, $\beta = 5$

$V = 0.09 \; [L/s]$

(b) gait $G2$

Experimental results (Gait $G4$): $A = 25$, $\psi = 40$, $\omega = 60$, $\beta = 5$
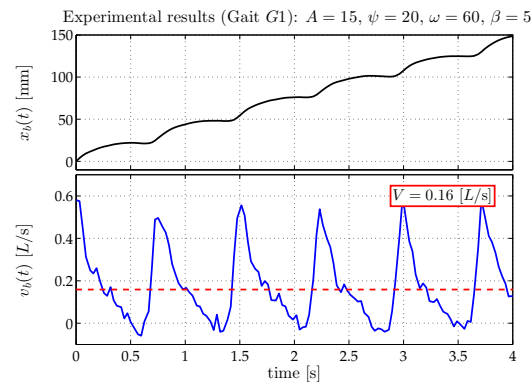
$V = 0.13 \; [L/s]$

(c) gait $G4$

Fig. 13: Experimental results for the horizontally constrained 8-arm prototype with rigid arms: Displacement and axial velocity (normalized by the arm length L), for gaits $G1$, $G2$, and $G4$. The dashed red line indicates the average velocity.

Experimental results (Gait $G1$): $A = 15$, $\psi = 20$, $\omega = 60$, $\beta = 5$

$V = 0.16 \; [L/s]$

(a) gait $G1$

Experimental results (Gait $G2$): $A = 15$, $\psi = 20$, $\omega = 60$, $\beta = 5$

$V = 0.17 \; [L/s]$

(b) gait $G2$

Experimental results (Gait $G4$): $A = 15$, $\psi = 20$, $\omega = 60$, $\beta = 5$

$V = 0.20 \; [L/s]$

(c) gait $G4$

Fig. 14: Experimental results for 8-arm prototype with rigid arms, swimming freely: Displacement and axial velocity (normalized by the arm length L), for gaits $G1$, $G2$, and $G4$. The dashed red line indicates the average velocity.

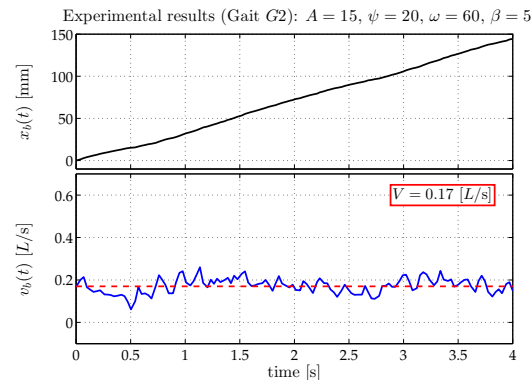simultaneously moving arms in each of those gaits.

B. Free-swimming propulsion results

The experiments with the prototype swimming freely, propelled both by rigid and compliant arms, demonstrated that the investigated gaits G1, G2, and G4, are capable of providing forward movement along a fairly straight path (see accompanying video).
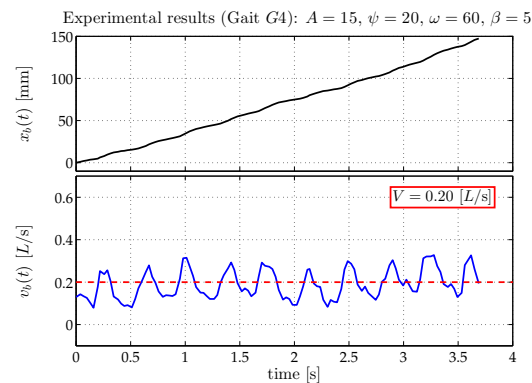
Regarding the prototype with the rigid arms, the velocity profile plots for all three gaits (Fig. 14), also exhibit the qualitative characteristics found in the simulation results.

Further, it is noted that the average attained velocity was similar for the three gaits, a finding which is consistent with the simulations, and which reinforces the reasoning presented in Section VI-A regarding the effect of friction. Moreover, the magnitude of this average velocity (approximately 0.19 L/s) is reasonably close to the one predicted by the simulation (approximately 0.26 L/s, cf. Fig. 8), especially when taking into account effects such as the influence of the interconnecting cables (which hindered the motion to some extend), imperfect buoyancy compensation, and the inher-
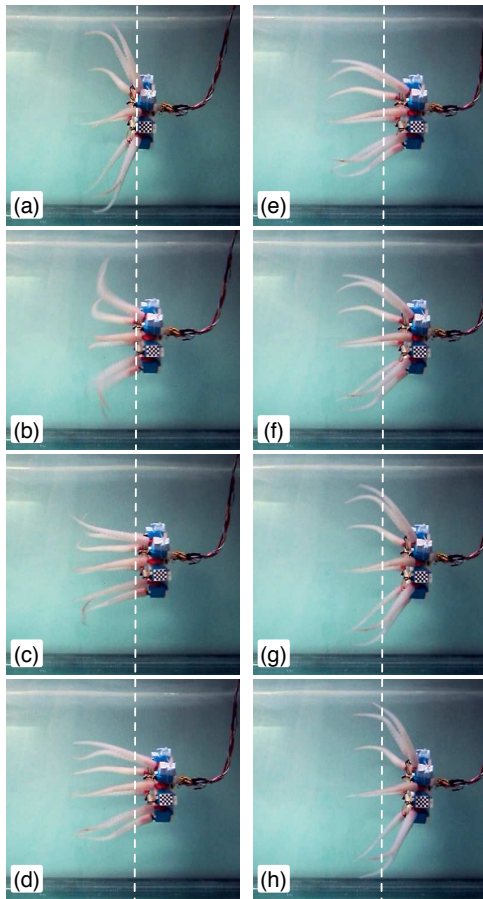
Fig. 15: Experimental results of free swimming with compliant arms, for gait $G1$ ($A = 25°$, $\psi = 40°$, $\omega = 60°/sec$, $\beta = 5$). Dashed line indicates the initial position of the prototype in (a). Frames are shown with a constant time interval of 135 ms. Frames (a)-(c) correspond to the power stroke and (d)-(h) to the recovery stroke.

ent limitations of the servomotors, as well as performance variabilities among them.

With the use of the compliant arms, the realism of the motion was enhanced, as evident from the indicative results of one sculling period of gait G1 (Fig. 15), as well as from additional experiments with the other gaits.

VII. CONCLUSIONS

In the present paper, we studied the propulsive capabilities of an 8-arm robotic swimmer under various swimming gaits. Simulations predicted the generation of substantial propulsive forces for various swimming gaits, involving arm sculling and arm undulations, for forward and turning movements. Experiments with an 8-arm prototype were performed, first on a horizontally constraining rod, to assess various kinematic parameters, and then under unconstrained conditions, the arm was allowed to perform free swimming with both rigid and compliant arms. The experimental results showed similar trends to the simulation results.

The parametric studies focused primarily on gait $G1$, since this is the most biological relevant movement observed in the

octopus, and they identified the optimal parameters for obtaining maximum velocity. Moreover, the average velocities for gaits $G1$, $G2$ and $G4$ are similar, for identical parameters, which is supported by both the simulations and the free-swimming experiments. Future work will consider the extraction of detailed kinematic data from animal recordings and their implementation on the robotic swimmer, as well as the detailed investigation of movement with compliant arms and of turning movements.

VIII. ACKNOWLEDGMENTS

REFERENCES

[1] C. Huffard, "Locomotion by abdopus aculeatus (cephalopoda: Octopodidae): Walking the line between primary and secondary defenses," *J. Exp. Biol.*, vol. 209, pp. 3697– 3707, 2006.

[2] A. Kazakidi, M. Kuba, A. Botvinnik, M. Sfakiotakis, T. Gutnick, S. Hanassy, G. Levy, J. A. Ekaterinaris, T. Flash, B. Hochner, and D. P. Tsakiris, "Swimming patterns of the octopus vulgaris," *22nd Annual Meeting NCM Society, April 23-29, Venice, Italy.*, 2012.

[3] Y. Gutfreund, T. Flash, Y. Yarom, G. Fiorito, I. Segev, and B. Hochner, "Organization of octopus arm movements: A model system for studying the control of flexible arms," *J. Neurosc.*, vol. 16, pp. 7297–7307, 1996.

[4] I. Walker, D. Dawson, T. Flash, F. Grasso, R. Hanlon, B. Hochner, W. Kier, C. Pagano, C. Rahn, and Q. Zhang, "Continuum robot arms inspired by cephalopods," in *Proc. SPIE Conf. on Unmanned Ground Vehicle Technology IV*, vol. 5804, no. 37, 2005, pp. 303–314.

[5] C. Laschi, B. Mazzolai, V. Mattoli, M. Cianchetti, and P. Dario, "Design of a biomimetic robotic octopus arm," *Bioinspir. Biomim.*, vol. 4, no. 1, pp. 015 006–1–8, 2009.

[6] R. Kang, A. Kazakidi, E. Guglielmino, D. Branson, D. Tsakiris, J. Ekaterinaris, and D. Caldwell, "Dynamic model of a hyper-redundant, octopus-like manipulator for underwater applications," in *Proc. IEEE/RSJ Int. Conf. on Int. Rob. Syst. (IROS'11)*, 2011.

[7] M. Sfakiotakis, A. Kazakidi, N. Pateromichelakis, J. Ekaterinaris, and D. P. Tsakiris, "Robotic underwater propulsion inspired by the octopus multi-arm swimming," *IEEE Int. Conf. Rob. Autom. (ICRA'12)*, 2012.

[8] J. Mather, "How do octopuses use their arms?" *J. Comparative Psychology*, vol. 112, no. 3, pp. 306–316, 1998.

[9] A. Kazakidi, V. Vavourakis, N. Pateromichelakis, J. Ekaterinaris, and D. P. Tsakiris, "Hydrodynamic analysis of octopus-like robotic arms," *IEEE Int. Conf. Rob. Autom. (ICRA'12)*, pp. 5295–5300, 2012.

[10] J. Jeong and F. Hussain, "On the identification of a vortex," *J. Fluid Mech.*, vol. 285, pp. 69–94, 1995.

[11] G. Taylor, "Analysis of the swimming of long and narrow animals," *Proc. Roy. Soc. A*, vol. 214, pp. 158–183, 1952.

[12] Ö. Ekeberg, "A combined neuronal and mechanical model of fish swimming," *Biol. Cybern.*, vol. 69, no. 5-6, pp. 363–374, 1993.

[13] A. Ijspeert, "A connectionist central pattern generator for the aquatic and terrestrial gaits of a simulated salamander," *Biol. Cybern.*, vol. 85, no. 5, pp. 331–348, 2001.

[14] K. A. McIsaac and J. P. Ostrowski, "Experimental verification of open-loop control for an underwater eel-like robot," *Int. J. Rob. Res.*, vol. 21, pp. 849–860, 2002.

[15] M. Sfakiotakis and D. P. Tsakiris, "Biomimetic centering for undulatory robots," *Intl. J. Rob. Res.*, vol. 26, pp. 1267–1282, 2007.

[16] M. Sfakiotakis and D. P. Tsakiris, "Undulatory and pedundulatory robotic locomotion via direct and retrograde body waves," *IEEE Int. Conf. Rob. Autom. (ICRA'09)*, pp. 3457–3463, 2009.

[17] Z. Zhang, "Flexible camera calibration by viewing a plane from unknown orientations," *Proc. IEEE Int. Conf. on Comp. Vision (ICCV'99)*, pp. 666–673, 1999.